Targeting structural flexibility in low density lipoprotein by integrating cryo-electron microscopy and high-speed atomic force microscopy

Aline Cisse, Ambroise Desfosses, Sarah Stainer, Eaazhisai Kandiah, Daouda Traore, Armel Bezault, Anna-Laurence Schachner-Nedherer, Gerd Leitinger, Gerd Hoerl, Peter Hinterdorfer, et al.

International Journal of Biological Macromolecules 252 (2023) 126345

Contents lists available at ScienceDirect

International Journal of Biological Macromolecules

journal homepage: www.elsevier.com/locate/ijbiomac

Targeting structural flexibility in low density lipoprotein by integrating cryo-electron microscopy and high-speed atomic force microscopy

Aline Cisse [a,b], Ambroise Desfosses [c], Sarah Stainer [d], Eaazhisai Kandiah [e], Daouda A.K. Traore [b,f,g], Armel Bezault [h,i], Anna-Laurence Schachner-Nedherer [j], Gerd Leitinger [k], Gerd Hoerl [l], Peter Hinterdorfer [d], Irina Gutsche [c], Ruth Prassl [j], Judith Peters [a,b,m,*], Karin Kornmueller [b,j,*]

[a] Université Grenoble Alpes, CNRS, LiPhy, Grenoble, France
[b] Institut Laue-Langevin, Grenoble, France
[c] Institut de Biologie Structurale, Université Grenoble Alpes, CEA, CNRS, IBS, Grenoble, France
[d] Department of Experimental Applied Biophysics, Johannes Kepler University Linz, Linz, Austria
[e] European Synchrotron Radiation Facility, Grenoble, France
[f] Faculté de Pharmacie, Université des Sciences, des Techniques et des Technologies de Bamako (USTTB), Bamako, Mali
[g] Faculty of Natural Sciences, School of Life Sciences, Keele University, Staffordshire, UK
[h] Institut Européen de Chimie et Biologie, UAR3033/US001, Université de Bordeaux, CNRS, INSERM 2, Pessac, France
[i] Structural Image Analysis Unit, Department of Structural Biology and Chemistry, Institut Pasteur, Université Paris Cité, CNRS UMR3528, Paris, France
[j] Gottfried Schatz Research Center for Cell Signaling, Metabolism and Aging, Medical Physics and Biophysics Division, Medical University of Graz, Graz, Austria
[k] Gottfried Schatz Research Center for Cell Signaling, Metabolism and Aging, Division of Cell Biology, Histology and Embryology, Medical University of Graz, Graz, Austria
[l] Otto Loewi Research Center, Physiological Chemistry, Medical University of Graz, Graz, Austria
[m] Institut Universitaire de France, France

ARTICLE INFO

Keywords:
Low density lipoprotein
LDL
Apolipoprotein B-100
Apo B-100
Cryo-electron microscopy
High speed atomic force microscopy
Flexibility

ABSTRACT

Low-density lipoprotein (LDL) plays a crucial role in cholesterol metabolism. Responsible for cholesterol transport from the liver to the organs, LDL accumulation in the arteries is a primary cause of cardiovascular diseases, such as atherosclerosis. This work focuses on the fundamental question of the LDL molecular structure, as well as the topology and molecular motions of apolipoprotein B-100 (apo B-100), which is addressed by single-particle cryo-electron microscopy (cryo-EM) and high-speed atomic force microscopy (HS-AFM). Our results suggest a revised model of the LDL core organization with respect to the cholesterol ester (CE) arrangement. In addition, a high-density region close to the flattened poles could be identified, likely enriched in free cholesterol. The most remarkable new details are two protrusions on the LDL surface, attributed to the protein apo B-100. HS-AFM adds the dimension of time and reveals for the first time a highly dynamic direct description of LDL, where we could follow large domain fluctuations of the protrusions in real time. To tackle the inherent flexibility and heterogeneity of LDL, the cryo-EM maps are further assessed by 3D variability analysis. Our study gives a detailed explanation how to approach the intrinsic flexibility of a complex system comprising lipids and protein.

1. Introduction

Low-Density Lipoprotein (LDL) acts as the main cholesterol transporter in blood circulation. LDL's hydrophilic shell is composed of a phospholipid monolayer and a single amphipathic apolipoprotein B-100 (apo B-100) molecule, with a molecular mass of about 550 kDa [1,2]. In its core, LDL encompasses various types of hydrophobic elements, such as cholesterol in its free and esterified form, as well as triglycerides [3,4].

It was recognized that a high concentration of LDL in the plasma is a risk factor in cardiovascular diseases [5–9]. Indeed, the onset of many cardiovascular diseases, like atherosclerosis, is marked by a steady accumulation of LDL in the arterial walls [10]. Often, modified forms of LDL, like triglyceride-rich or oxidatively modified LDL, are involved in this process [11–16]. Nevertheless, the molecular properties of LDL,

* Corresponding authors at: Medical University of Graz, Graz, Austria and Institut Laue-Langevin, Grenoble, France.
E-mail addresses: jpeters@ill.fr (J. Peters), karin.kornmueller@medunigraz.at (K. Kornmueller).

https://doi.org/10.1016/j.ijbiomac.2023.126345
Received 11 May 2023; Received in revised form 8 August 2023; Accepted 13 August 2023
Available online 22 August 2023

Abbreviations

apo B-100	apolipoprotein B-100
CE	cholesterol ester
cryo-EM	cryo-electron microscopy
CTF	contrast transfer function
FSC	Fourier Shell Correlation
HS-AFM	high-speed atomic force microscopy
LDL	low density lipoprotein
MSD	mean square displacement
SANS	small angle neutron scattering
VLDL	very low density lipoprotein

which are inherently related to its binding properties and cellular recognition, still contain open questions, such as the precise molecular structures of LDL and apo B-100. LDL's structural features have been studied since the 70s using cutting-edge techniques like small-angle X-ray or neutron scattering [17–26], X-ray crystallography [27,28], incoherent neutron scattering [29–31], or electron microscopy [32–41]. Cryo-EM offers the advantage of directly imaging close to native, vitrified LDL particles, though the 3D reconstruction and interpretation of cryo-EM maps remains challenging. One obstacle is that LDL is a complex assembly of lipids and protein. Both of them have similar electron cross-sections, resulting in hardly distinguishable electron densities [17]. Slight differences reside in the denser rings of cholesterol in its free or esterified forms (around 0.42 e^-/nm^3) and in the phospholipids' headgroups which have slightly stronger densities (about 0.40–0.45 e^-/nm^3) than their acyl chains (0.29 e^-/nm^3) [17]. These visual differences, seen in an early cryo-EM map of LDL [35], led to a paradigm shift in the understanding of the core organization. Instead of a radial distribution of cholesterol esters (CE) in the core [42,43], the prevailing model is now a lamellar arrangement of CE molecules below the lipoprotein's core lipid transition. More precisely, LDL undergoes a fully reversible temperature-induced transition from a liquid-crystalline to a liquid disordered state of the core lipids. Depending on the CE to triglyceride ratio, the transition temperature ranges from 19 to 32 °C [44]. At temperatures below this phase transition, CE packing results in planar layers, seen as characteristic striations in cryo-EM images. Above the phase transition, the core shows an anisotropic distribution of CE molecules. An approach to capture the core organization above the phase transition temperature by cryo-EM resulted in a low-resolution map that indeed lacked the characteristic CE planes due to a disordered lipid packing combined with increased lipid flexibility and mobility [38].

The molecular structure of apo B-100 is still a matter of intense research. Its secondary structure is commonly described by a computationally derived "pentapartite" model, where the protein is divided into five consecutive domains: NH_2-$\beta\alpha_1$-β_1-α_2-β_2-α_3-COOH [45,46], with α (α-helices) or β (β-sheets) being the major conformational motifs. Mapping the individual domains onto the LDL particle was approached by several groups computationally [47] or with cryo-EM [37,38,40,41]. For example, LDL was imaged in complex with a part of its receptor (LDLr), from which the location for the possible receptor-binding site on LDL was proposed [37]. Labelling of apo B-100 with gold nanoparticles [40] or selective labelling of individual domains with monoclonal antibodies [32,39,41] revealed the rough topology of apo B-100 on the LDL surface. There is a wide consensus that apo B-100 wraps around the LDL surface like a belt and that the NH_2 and COOH termini are in close proximity. The $\beta\alpha_1$ domain (i.e. the first 1000 amino acids of the N-terminal region) is structurally well described due to its homology to lipovitellin [48,49]. Within this region, the first 5.9 % of the N-terminal domain extend as a β-barrel protrusion [40,41]. In physiology, the $\beta\alpha_1$ domain plays an important role in the process of lipoprotein assembly and secretion [50,51]. Concurrently with apo B-100 mRNA translation, lipoprotein assembly starts at the ER membrane. The $\beta\alpha_1$ domain directly interacts with lipids and serves as first contact site where lipids are directed to. In addition, the $\beta\alpha_1$ domain interacts with the chaperone microsomal triglyceride transfer protein (MTP), which also has homology to lipovitellin. The β-barrel of apo B-100 is a docking site for MTP where a triangular pocket is formed that enhances lipid transfer and thus the chaperone shuffles a greater number of lipids towards apo B-100. The whole initiation process of lipoprotein assembly critically depends on proper folding of the apo B-100 N-terminal domain, lipid availability and MTP [50,51].

Since pioneering cryo-EM studies on LDL in the 90s [34,35] and the latest approaches in 2011 [37,38,40,41], the cryo-EM technique has gone through considerable improvements, especially concerning the detectors and algorithms for image processing, reaching in some cases atomic resolution [52–54]. During the last few years, many membrane proteins have been investigated by cryo-EM, as reviewed in [55–57], and more often also in presence of a lipid bilayer, whether it be from nanodiscs [58,59] or liposomes [60]. Nevertheless, it is important to keep in mind that a cryo-EM model is a static representation of a biomolecule that is naturally in motion. Thus, every model represents an average of different molecular conformations, captured in a single snapshot. In cryo-EM it is challenging to resolve features of flexible domains that are typically blurred or lost. In practice, structural flexibility is addressed by large dataset processing, and by using current algorithms of classification or variability estimation (like CryoSparc 3DVA or CryoDRGN [61,62]).

In contrast to cryo-EM, high-speed atomic force microscopy (HS-AFM) offers the possibility to directly capture the motions of a biomolecule with nanometer spatial resolution and millisecond temporal precision [63]. LDL has been the target of classical AFM-studies, mostly by assessing its size [64,65] or its biomechanical properties [66,67]. However, the intrinsic dynamics of LDL has never been recorded and visualized by HS-AFM before.

In this study we combined both techniques, cryo-EM and HS-AFM. We addressed the fundamental question of the structure and inner organization of LDL particles, and simultaneously set a focus on its intrinsic flexibility. By cryo-EM, we could identify regions that appeared highly conserved and others that showed large flexibility. By HS-AFM we were able to directly observe movements of individual protein domains on a millisecond timescale. Evident by both techniques, we could identify several protrusions of the protein on the LDL surface, where only one protrusion has been reported before [40,41]. Though poorly resolved in the cryo-EM model, the protrusions and their associated dynamics were well described by HS-AFM. In contrast, the lipid core was exceptionally well resolved by cryo-EM, which gave rise to a revised model of the CE organization.

2. Results

We examined a highly homogeneous subfraction of LDL ($\rho = 1.0286 \pm 0.004$ g/cm^3) using cryo-EM. A total of ~15 k micrographs was collected and processed using Relion and cryoSPARC. In several rounds of 2D classification ~700 k LDL particles were extracted (see Methods and Fig. S1) and 2D class averages of particles with distinctive structural features (top view, layered side view, protrusions) were selected and processed to obtain a 3D consensus map at a resolution of 9 Å (FSC 0.143 criteria). Fig. 1 shows an example of a raw micrograph (Fig. 1A) and a selection of the most representative 2D classes (Fig. 1B-D).

Fig. 2 shows the LDL cryo-EM consensus map. Overall, the LDL model exhibits dimensions of 16 nm in height and ~ 22 nm in diameter. Its opposite flat surfaces are designated as the poles, or "top" and "bottom" of the LDL. When viewed from the front, it presents a rounded rectangular shape, similar to earlier cryo-EM maps [37–41]. Evident is a layered organization of the LDL core, which is an effect of CE molecule arrangement in their crystalline phase below LDLs phase transition temperature [24,25,39]. The individual layers are separated by about

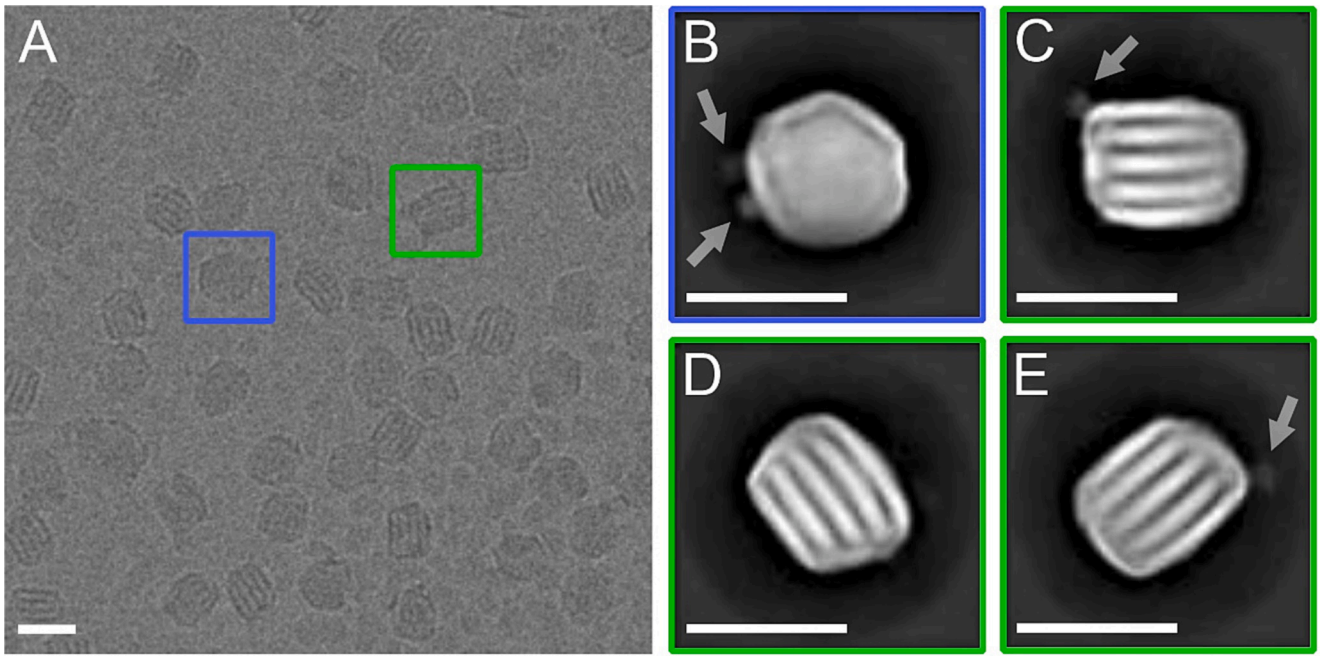

Fig. 1. LDL cryo-EM. A: Example of a cryo-EM collected micrograph. The blue box highlights a typical LDL particle viewed from the top, the green box shows an example of a side view. Scale bar: 20 nm. B-E: Examples of 2D classes of LDL particles processed in cryoSPARC (400 × 400 pixels box). The arrows highlight visible protrusions. Scale bar: 20 nm. (For interpretation of the references to colour in this figure legend, the reader is referred to the web version of this article.)

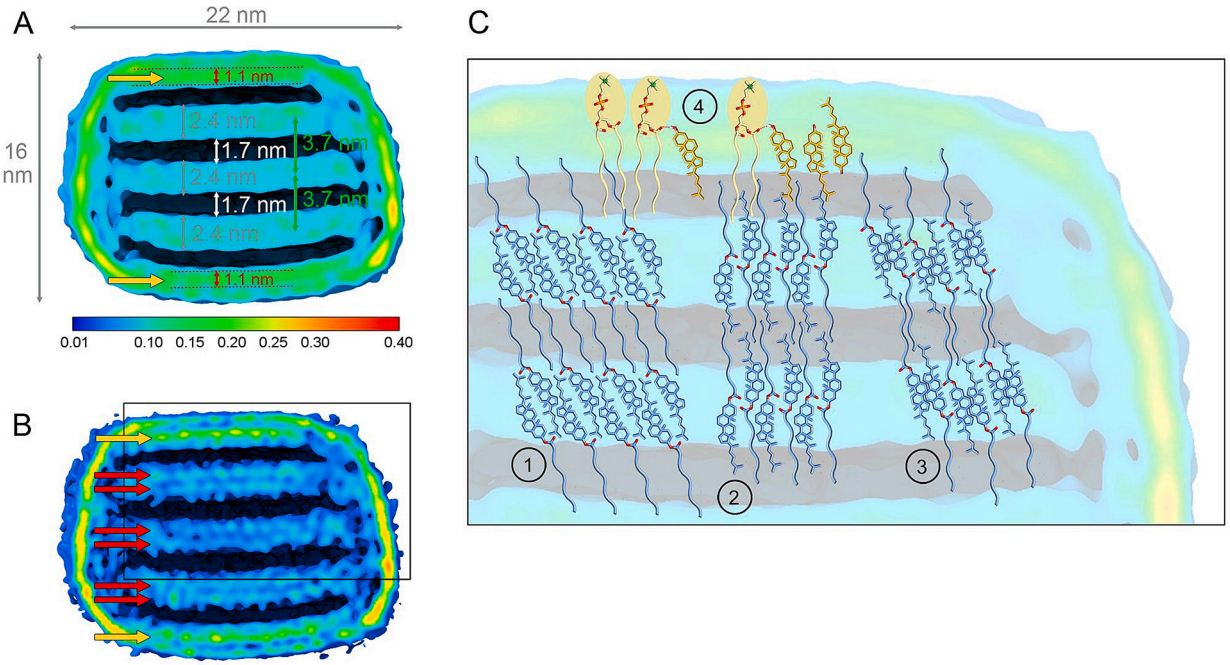

Fig. 2. Cross-section through the LDL cryo-EM consensus map. A: Unsharpened cryoSPARC map, indicating the internal organization and regions of interest of LDL. The map was coloured according to the density map values using UCSF ChimeraX [68,69]. B: The sharpened map enhances distinct structural features (see arrows). The three sets of parallel red arrows highlight a substructured arrangement of the three CE layer planes. The yellow arrows close to the poles highlight two electron-dense regions that we assign to an area where preferentially free cholesterol molecules accumulate. C: Three models are proposed how CE molecules might arrange within the characteristic substructured layers. Model 4 highlights the coordination of free cholesterol with a phospholipid. The sterol rings of cholesterol are expected to give the highest contrast and thus being responsible for the high densities within the CE layers in models 1–3. The models are based on information on the crystal structures of isolated systems of the most prevailing CEs in LDL, additionally taking into account geometric considerations. Model 1 and 2 are based on the interdigitated bilayer arrangement of cholesterol-palmitate [70,71], model 3 is based on the monolayer type II crystal system of cholesteryl-oleate [70]. (For interpretation of the references to colour in this figure legend, the reader is referred to the web version of this article.)

3.7 nm (see Fig. 2A), which is consistent with the 3.6 nm periodic spacing previously measured and estimated with SAXS [19,24,25] or cryo-EM [37,39,40]. What is new - and even more apparent in the post-processed map shown in Fig. 2B - are the fine substructures within the three CE planes. Our map reveals that each plane can be roughly divided into two planes of higher density (indicated by two red arrows in

Fig. 2B), intermitted by a region with lower density. Until now, the CE planes were presented only with a homogeneous density distribution [37]. We see for the first time that - within the two layers of one CE plane - also microdomains of higher density can be distinguished. We attribute this higher density to the sterol rings of CE molecules, which are ~1 nm in size.

We posed ourselves the question how the CE molecules might be organized in the light of these new findings. The predominant CE-species in LDL is cholesteryl linoleate (linoleic acid, C18:2) making up ~55 % of the CEs, followed by cholesteryl oleate (oleic acid, C18:1) with ~17 %, and cholesteryl palmitate (palmitic acid, C16:0) with ~16 % [72]. As depicted in Fig. 3, in isolated systems cholesteryl-palmitate self-assembles into bilayers, where the acyl chains are interdigitated [70,71]. Cholesteryl-oleate forms monolayer type II crystals, with a tight antiparallel packing of the sterol rings [70]. Cholesteryl-linoleate has no reported crystal structure, probably because of its double unsaturation [70]. Based on this information and geometric considerations (taking into account the volume of CE molecules and the available space to occupy), we here propose 3 models how CE molecules within the core might be arranged. Two models take the cholesteryl-palmitate bilayer arrangement as reference, one with a strong interdigitation of the cholesterol head (i.e. the sterol rings and the cholesterol hydrocarbon tail, Fig. 2C ①), one without cholesterol head interdigitation (Fig. 2C ②). The CE acyl chains are in all cases interdigitated, given the limited space of the 1.7 nm low density regions, where we expect the CE acyl chains to prevail. The third model is based on a monolayer arrangement as seen for cholesteryl-oleate, with strong antiparallel packing of the sterol rings (Fig. 2C ③). Respecting the fact that the majority of CE molecules is cholesteryl-linoleate, and that we must not neglect the presence of free cholesterol and triacylglycerol in the core, a combination of all models seems very likely. This might be best described by a raft-like/domain-like arrangement, where CE molecules of the same species form local clusters. The fact that we observe patches of denser and less dense regions within one CE plane corroborates this notion.

A high-density region can be found close to the two poles (indicated by yellow arrows in Fig. 2A and B). The poles are supposed to contain predominantly phospholipids, being an area relatively free of protein. Phospholipids are well known to interact with cholesterol, with a hydrogen bond (~ 0.18–0.34 nm) between the oxygen of the cholesterol hydroxyl group and the lipid ester oxygen or the lipid phosphate oxygen [74,75]. Due to this typical coordination, the cholesterol molecule is shifted towards the phospholipid tail region [74] (see Fig. 2C ④). It was already suggested that 2/3 of the total free cholesterol concentrates within the shell [3,4], a finding that was also supported by MD simulations [76]. Thus, we presume that the majority of free cholesterol (with its sterol rings of ~1 nm and a considerably higher electron density than phospholipids) preferentially accumulates exactly within this high-density layer close to the poles (see Fig. 2C ④).

The most striking new detail within the shell in the cryo-EM map of LDL is the presence of two protrusions, one of which has never been observed before (Fig. 4), and discontinuities in the shell lipid densities (see Fig. S2). We termed the two protrusions arbitrarily “front” and “side” protrusion, with respect to their localization on the LDL particle. In many 2D classes either one or both protrusions are visible (see arrows in Fig. 1B-E). The “front” protrusion is quite prominent and was already assessed by some of the previous cryo-EM studies [37–41]. This protrusion is commonly associated with the globular NH_2-$\beta\alpha_1$ domain of the apo B-100 protein, and there with the first ~270 amino acids [41]. On the contrary, the second protrusion is described here for the first time. The reason why we were able to see this second protrusion is most likely a combination of several factors: the technical advances towards better microscopes together with better alignment procedures and software, and most importantly a larger data collection that boosts up the occurrence of LDL particles with the protrusion.

Successive 3D classifications resulted in three different maps, which are depicted in Fig. 4. In all three classes, the global shape remains similar, but slight differences are concentrated on the regions of the protrusions and are manifest in the presence of either one (the “front” (F) or “side” (S)), or both (SF) protrusions. An in-depth characterization was done with the SF map, showing both protrusions (Fig. 5). The “front” protrusion (Fig. 5, plain ellipse) is characterized by three vertical lines, each one with a length between 2 nm and 3.5 nm (as seen in the inset of Fig. 5B). From the left view (Fig. 5A), the “front” protrusion has a triangular shape, with a base of about 4.5 nm and a height of around 2.4 nm. In contrast, the “side” protrusion (Fig. 5, dashed ellipse) is less globular in its shape: as highlighted in Fig. 5A and B, the extra densities are aligned along a vertical line, estimated to be around 9 nm. From the top, this protrusion appears much thinner, extending only ~2 nm from the LDL surface. The “side” protrusion is about 13 nm apart from the “front” protrusion, as depicted in Fig. 5A by the red arrow.

The presence of protrusions is also clearly visible in high-speed atomic force microscopy (HS-AFM) recordings. Analysis of the HS-AFM dataset suggests that zero to three protrusions emerge from each LDL particle (Fig. 6). From $N = 21$ LDL particles observed, 33.3 % showed no (visible) protrusion, 33.3 % one protrusion, 14.3 % two protrusions and 19 % three protrusions. The LDL particle seems to take a preferential orientation on the mica, with its flattened poles parallel to the mica surface. Topographical analysis suggests this orientation (Fig. S3), since we reproducibly measured heights of 14.0–17.1 nm, which correspond well to a pole-to-pole distance of ~16 nm in the cryo-EM map. Also, the measured LDLs total diameter of 20.6–25.0 nm is well in accordance with the consensus of a typical LDL diameter with a size

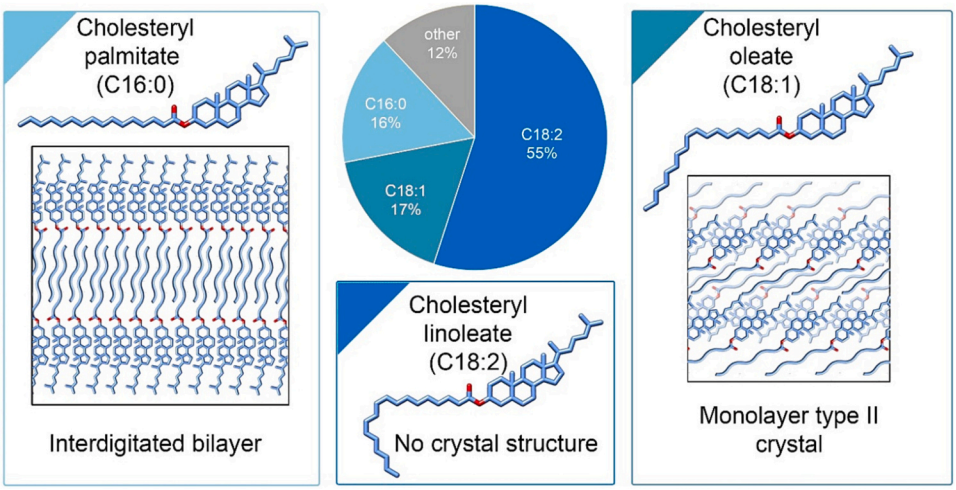

Fig. 3. CE arrangement. The most prevailing CEs in LDL [72] are shown, together with their crystal structures in isolated systems [70,71]. Cholesteryl-linoleate is most abundant (55 %) but does not form crystals as isolated CE species. Cholesteryl-oleate accounts for ~17 % of all CEs in LDL and forms a monolayer type II crystal structure when being isolated. Cholesteryl-palmitate accounts for ~16 % and forms an interdigitated bilayer. The structures served as basis for understanding the CE arrangement in the LDL core. The molecular structures of the individual CEs were accessed from PubChem [73](Compound CIDs: 246520, 5287939, 5283632).

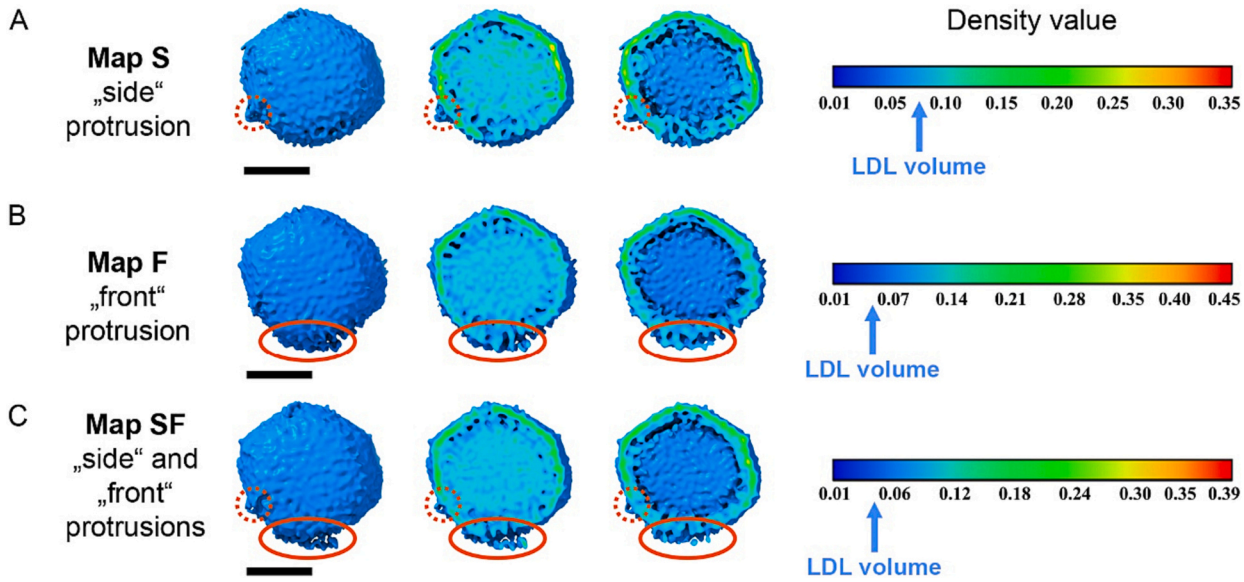

Fig. 4. Final 3D classes in cryoSPARC. The top view of the LDL map is shown, as well as two horizontal cuts, the first one through a CE layer plane, the second one below a CE layer plane. A: Map S highlights the "side" protrusion, populated with 150 k particles. B: Map F shows the "front" protrusion, with 272 k particles. C: Map SF shows the "side" and the "front" protrusion, with 258 k particles. Scale bar: 10 nm. 3D map images were produced with UCSF ChimeraX [68,69].

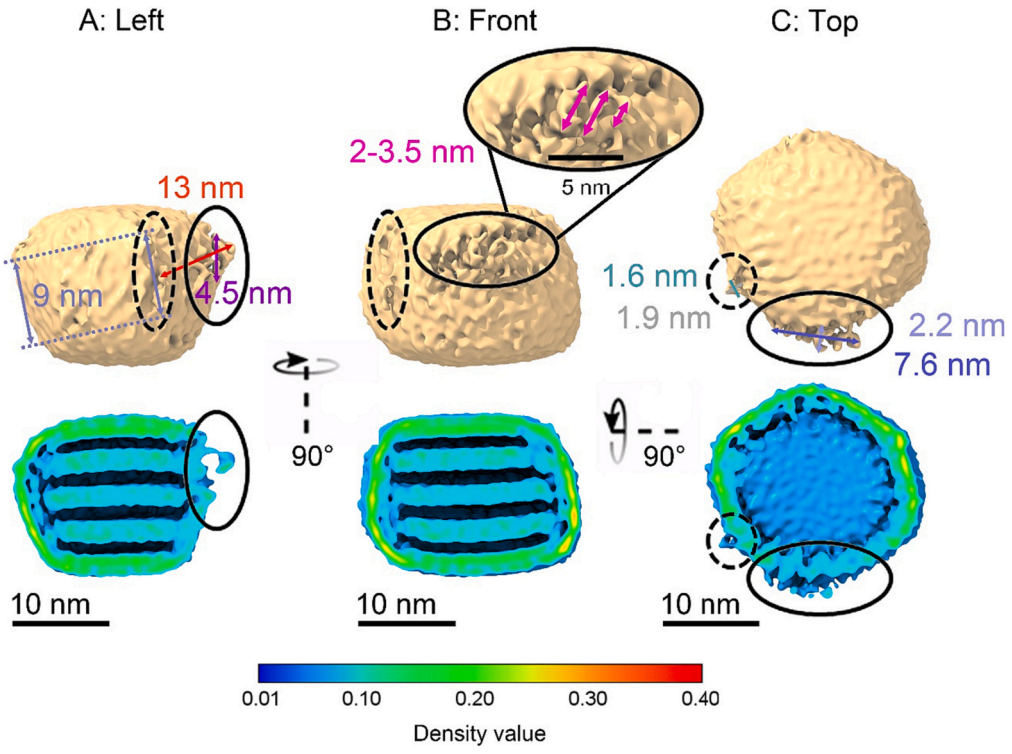

Fig. 5. Protrusion characterization in the cryo-EM map. LDL shows two characteristic protrusions. The 3D map of LDL derived from cryoSPARC, with different views shown in the first row and the corresponding middle cut through the LDL particle in the second row. A: Left view. B: Front view, with an inset zooming on the front protrusion. C: Top view. The plain ellipse circles the "front" protrusion, and the dashed circle the "side" protrusion. Maps are coloured according to the density value, whose legend is shown below. Scale bar: 10 nm. 3D map images were produced with UCSF ChimeraX [68,69].

range around 18–25 nm, and an average particle diameter of ~22 nm [2]. Only LDL with three protrusions seems to mark an exception: these particles show a significantly smaller size of the core particle (i.e. only the quasi-spherical shaped part), compared to LDL with zero, one or two protrusions. The statistical analysis of the LDL dimensions is summarized in Table 1 and shown in Fig. S3. Considering that the geometry of the AFM-tip causes broadening in the scanning direction [77], all AFM-derived sizes were corrected assuming an AFM-tip-size of 2 nm.

A closer look into the individual protrusions suggests an averaged (N = 26) and tip effect corrected length of 10.2 ± 3.1 nm and a width of 5.1 ± 2.6 nm, where the protrusion length is measured along the protrusion's long axis and the width along its short axis (see Fig. S4 in the Supporting Material); cryo-EM-derived measurements of the area corresponding to the front protrusion suggest slightly smaller dimensions of ~8 nm × 2.2 nm. However, the dimension of the protrusions can only be considered as a rough estimate, since they move rapidly. Indeed, by tracking the mobility of the individual protrusions in HS-AFM recordings, we depicted the range of their motions (see movies S1 and S2 in the Supporting Material). The analysed protrusions (N = 6) cover an area in the range of ~13–182 nm^2 within an imaging time of 30 s

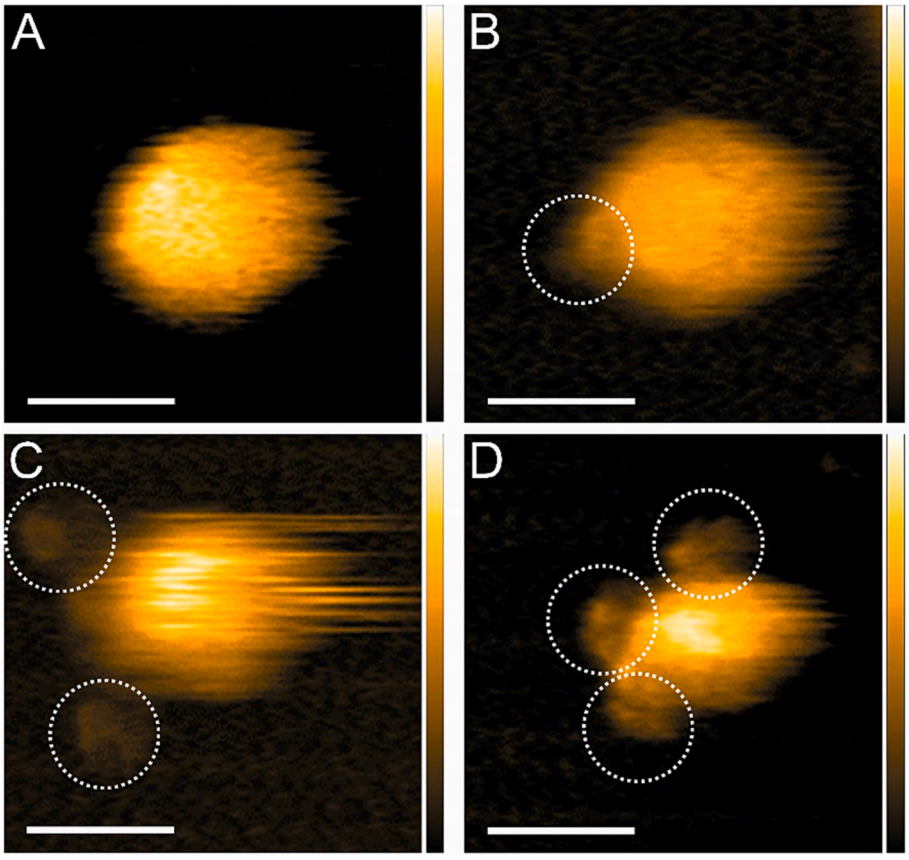

Fig. 6. HS-AFM recordings of LDL with different protrusion numbers. The characteristic quasi-spherical particles viewed from the top show either no visible protrusion (A), one (B and movie S3), two (C and movie S4) or three (D and movies S1 and S2) highly flexible protrusions. The protrusions are marked by circles, the scale bar corresponds to 25 nm, the z scale corresponds to 15 nm (A), 20 nm (B), 23 nm (C) and 10 nm (D).

Table 1
Tip effect corrected HS-AFM derived LDL dimensions with respect to the number of protrusions.

Number of protrusions	Occurrence (%)	LDL diameter (nm)	LDL height (nm)
0	33.3	25.0 ± 3.7	14.0 ± 1.4
1	33.3	24.9 ± 4.3	14.9 ± 1.8
2	14.3	20.6 ± 1.5	17.1 ± 0.7
3	19.0	17.6 ± 0.3	10.7 ± 2.2

$N = 21$.

(movies S1 and S2 in the Supporting Material). Fig. 7 and Fig. S5 show two selected LDL particles, each comprising three protrusions, and display the paths these three protrusions cover over time. In addition, an extraction of different conformations is shown in Fig. 8, again highlighting the variability in different conformations.

We attribute the motions observed by HS-AFM to domain fluctuations of apo B-100. Although we cannot directly link the individual protrusions to specific protein domains of apo B-100, our results are very well in line with the current consensus model of apo B-100. This computationally-derived model suggests 5 consecutive protein domains (NH_2-βα_1-β_1-α_2-β_2-α_3-COOH) that are connected by flexible linker regions, which favour motions relative to each other [21,46]. Parts of the protein are closely associated with the core region and are thus buried within the lipoprotein particle, whereas others are exposed to the surface, giving rise to higher flexibility. Taken together, HS-AFM gives a quite mobile picture of LDL – which emphasizes the need for further exploring LDL's conformational dynamics.

A means to access the flexible features of LDL with cryo-EM is variability analysis. By using 3DVA (cryoSPARC) and cryoDRGN, variability analyses were performed - the results of which are shown in Figs. 9 and 10. Both variability analyses point out considerable variations of the LDL shell, compared to a quite constant internal organization. Differences were mainly observed in the protrusion regions: presence or absence of the protrusions, extension from the LDL surface, or even partly disrupted structures from the shell. Nevertheless, the main limitations of both approaches are the need for a good estimation of the Euler angles as a starting point, and a 3D reference map that already presents secondary structure elements, which were so far impossible to obtain, due to the intrinsic LDL dynamics. Thus, the interpretation of the results must be taken with great care, but in general, they corroborate the 3D classification and HS-AFM results. The observed variations concentrated in the outer shell support the hypothesis of a great flexibility of the apo B-100 protein embedded in the LDL surface layer.

3. Discussion

There are two main sources that classify LDL as a challenging sample for structural analysis: sample heterogeneity and molecular motions within the particle. We aimed to overcome the intrinsic heterogeneity of LDL by a very restrictive sample preparation procedure, investigating only a highly purified density subfraction of LDL ($\rho = 1.0286 \pm 0.004$ g/cm^3). The exploration of molecular motions is still a challenge, and direct observation methods are scarce. It is certainly clear that we need to revise the static picture we have of many biomacromolecules. Nature is dynamic and the proteins inherent motions are equally linked to its function [78,79] as to its molecular structure. First hints of LDL's intrinsic flexibility can be derived from the comparison of our 3D map

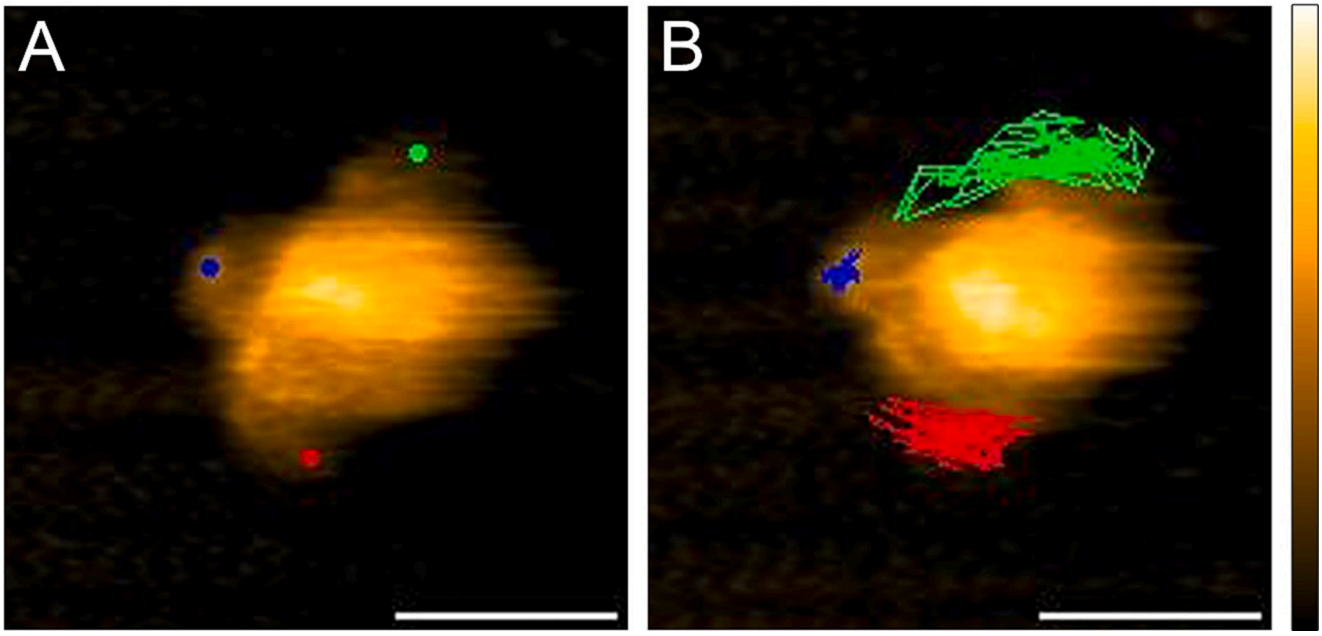

Fig. 7. Protrusion mobility tracking of an LDL particle showing three protrusions. The movie was recorded over 30 s. Scale bar: 25 nm, the z scale corresponds to 10 nm. Scanning speed: 239.59 ms/frame.

with an ab initio SANS model from [25], which is shown in Fig. S6 (Supporting Material). Despite similar shapes, the 3D model derived from the cryo-EM map is smaller than the SANS model, with up to 3 nm discrepancy. This difference is mostly explained by sample heterogeneity. For cryo-EM, a specific subfraction was used, whereas SANS studies were carried out on a lipoprotein fraction with a broader density range (comprising small dense to large buoyant LDL particles). However, it is interesting to note that the differences between both models derived from cryo-EM and SANS are not isotropic. Differences are less pronounced at the flattened poles and concentrate in the "belt" of LDL, often associated with apo B-100 regions. As noted from early LDL SANS experiments [20], the protein does not extend far beyond 1 nm from the phospholipids' surface, and it is very likely that our cryo-EM map "misses" some parts because of the protein's flexibility. Generally, in cryo-EM, highly flexible parts result in blurred densities, as seen for instance in [80–83], or in extreme cases in their total disappearance from the final map, like the central part of the nuclear pore complex [84,85].

It is still an open question why the total number of LDL protrusions we observed differed with respect to the experimental method. 3D classification in Cryo-EM yielded classes comprising only the "side", only the "front", or both protrusions. HS-AFM revealed the presence of none up to three protrusions. The absence of a third protrusion in the cryo-EM map might be explained by a combination of several factors: it might have a slightly larger flexibility, might be smaller in size, combined with a lower general prevalence. However, when we look at the protrusions from a different perspective – namely by looking at changes in the density distribution in the lipid shell of the cryo-EM map – we identify a third discontinuity in the lipid layer that might correspond to the location of a third protrusion. The different numbers of protrusions seen with HS-AFM might origin from the orientation of the LDL particle on the mica surface. For some particles (which show no obvious protrusion), we expect that there are protrusions that are not accessible by the AFM-tip, whether it is due to LDL's orientation on the mica or mica-protein interactions. We also suspect that a protrusion's position might vary also on a longer timescale than being observed with HS-AFM. This means that sometimes the protrusion might be closely attached to the LDL surface or even buried within the particle being not detectable with HS-AFM, sometimes it might be extending and being fully accessible. With HS-AFM we were able to directly follow conformational changes of LDL over several seconds. The observed motions can be attributed to fluctuations of the flexible domains of Apo B-100. In general, on even smaller time- and length scales one can observe quite localized dynamics of protein side-chain and backbone motions [79,86]. On the other end of the scale are motions of the entire protein. Rotation and translation of apo B-100 on LDL is highly influenced due to its embedding in a lipid environment. Our data from earlier neutron elastic scattering experiments supports the enhanced dynamics of lipoproteins. Mean square displacements (MSDs) of LDL and very low density lipoprotein (VLDL) are in a range of 2–3 $Å^2$ [29,30], whereas the MSDs of globular proteins are considerably smaller (~1 $Å^2$) [87].

The large flexibility of apo B-100 on the LDL surface is very well in line with its functionality. During the conversion from VLDL (> 50 nm) to LDL (22–30 nm) in lipoprotein metabolism, huge conformational changes are necessary, which are also reflected in the molecular dynamics, viscosities, fluctuations as well as motional coupling between apo-B100 and lipids being distinctly different between VLDL and LDL [29]. In addition, in a recent study we have shown that apo B-100 in its detergent-solubilized form exhibits a non-negligible internal diffusion propensity [88]. At the nanosecond time scale, its order of magnitude resembles those of centre-of-mass translational diffusion, and at the picosecond scale large dynamics and great flexibility comparable to lipids were detected [88]. The dynamics of apo B-100 on the LDL could be expected to be similar: highly constrained by their environment, but with significant internal dynamics, allowing adaptation to the various lipoproteins' sizes [89]. Taken together, apo B-100's flexibility is a crucial property of LDL – well in line with its function in metabolism, but still far from being fully understood.

4. Conclusion

We report in this paper new 3D reconstructions of LDL, using the state-of-the-art techniques cryo-EM and HS-AFM. Despite a challenging 3D reconstruction, due to the intrinsic complexity of the LDL particle, we contribute with our findings to the incremental collective process in elucidating the molecular structure of LDL. Our studies address the following main points: First, due to an improved resolution compared to the early 3D maps of LDL, the core- and shell organization of the lipids

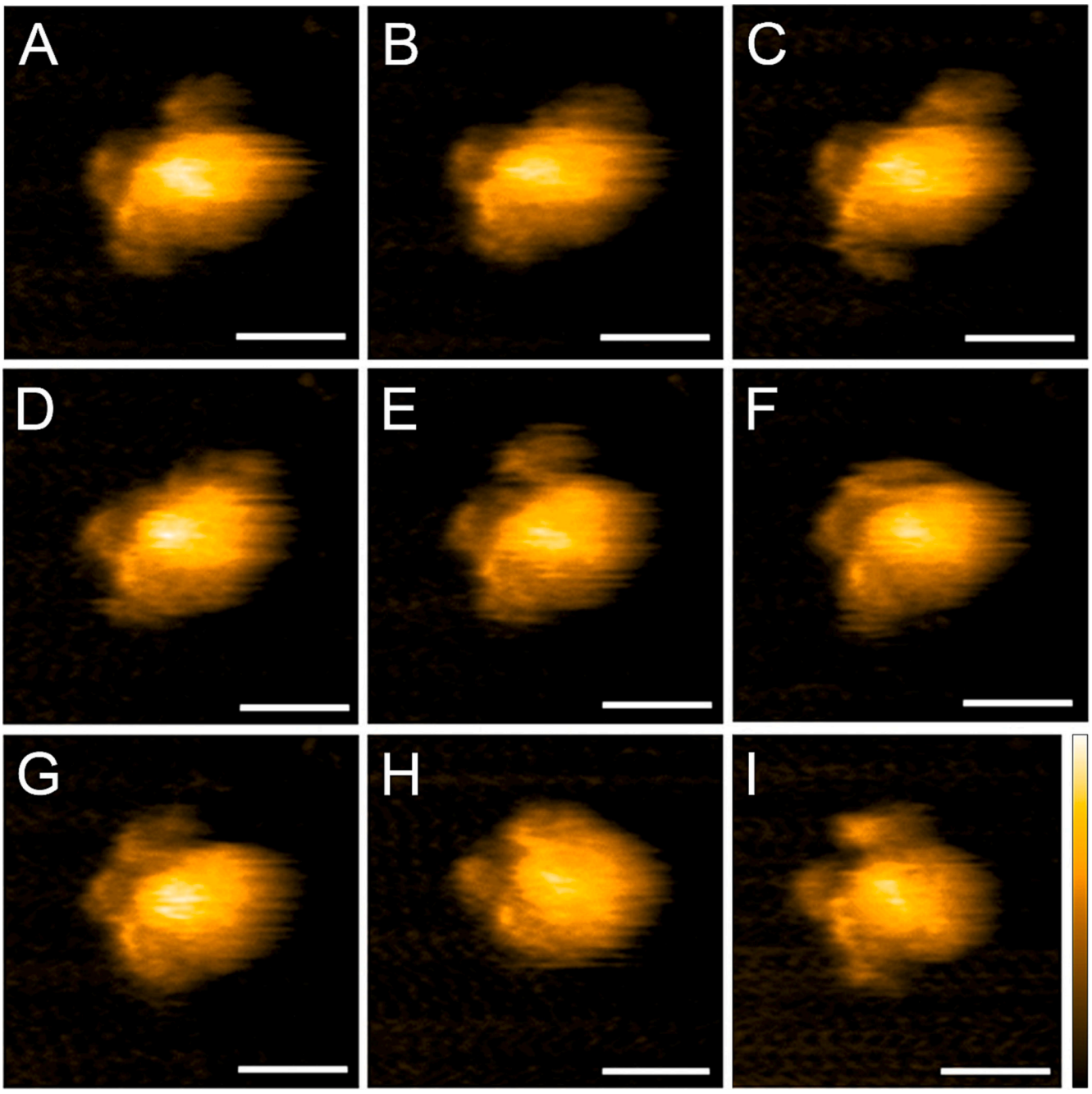

Fig. 8. A selection of different protrusion conformations recorded over time. The protrusions' movement is considerable and can adopt extended (e.g. A,C,E,I) or compact states (e.g. B,D,F.G,H). The scale bar corresponds to 25 nm, the z scale corresponds to 10 nm in all images.

are refined and novel details could be unveiled: we demonstrate a fine compartmentalisation of each CE plane, with two parallel planes of higher electron density, intermitted by a region of less density. In each plane the CE molecules might arrange as interdigitated bilayer or as several tightly packed antiparallel monolayer structures, however, most likely a combination of all architectures – in the form of a domain model. In addition, a region of high density is identified close to the flattened poles. We here expect free cholesterol being enriched, in a tight coordination with phospholipids, which shifts the cholesterol several nm towards the central core. Second, we could visualize two protrusions extending the maps, that we termed "front" and "side" protrusions, as well as discontinuities in the lipid layer, and attributed them to apo B-100. The largest one, displaying a globular shape, and positioned along the longest axis of the LDL, was associated with previous observations in cryo-EM and thus assigned to the NH_2-$\beta\alpha_1$ domain, notably the β-barrel, as compared to existing homologous models. The second protrusion, which was never assessed before, is located approximately 13 nm apart from the "front" protrusion and is characterized by an elongated 9 nm vertical appearance, extending only ~2 nm from the LDL surface. Despite the large dataset size and our efforts to isolate a homogeneous subset of LDL particles by classification methods, we could not resolve secondary structure elements of the protein. This is likely due to a large conformational heterogeneity of LDL, especially evident in the protrusion regions. HS-AFM allowed visualising the moving protein in millisecond time windows and underlined its extremely high flexibility. The metabolic conversion from VLDL to LDL requires large structural adaptations to the protein. Apo B-100 is an exception within the many apolipoproteins that are constantly exchanged within different

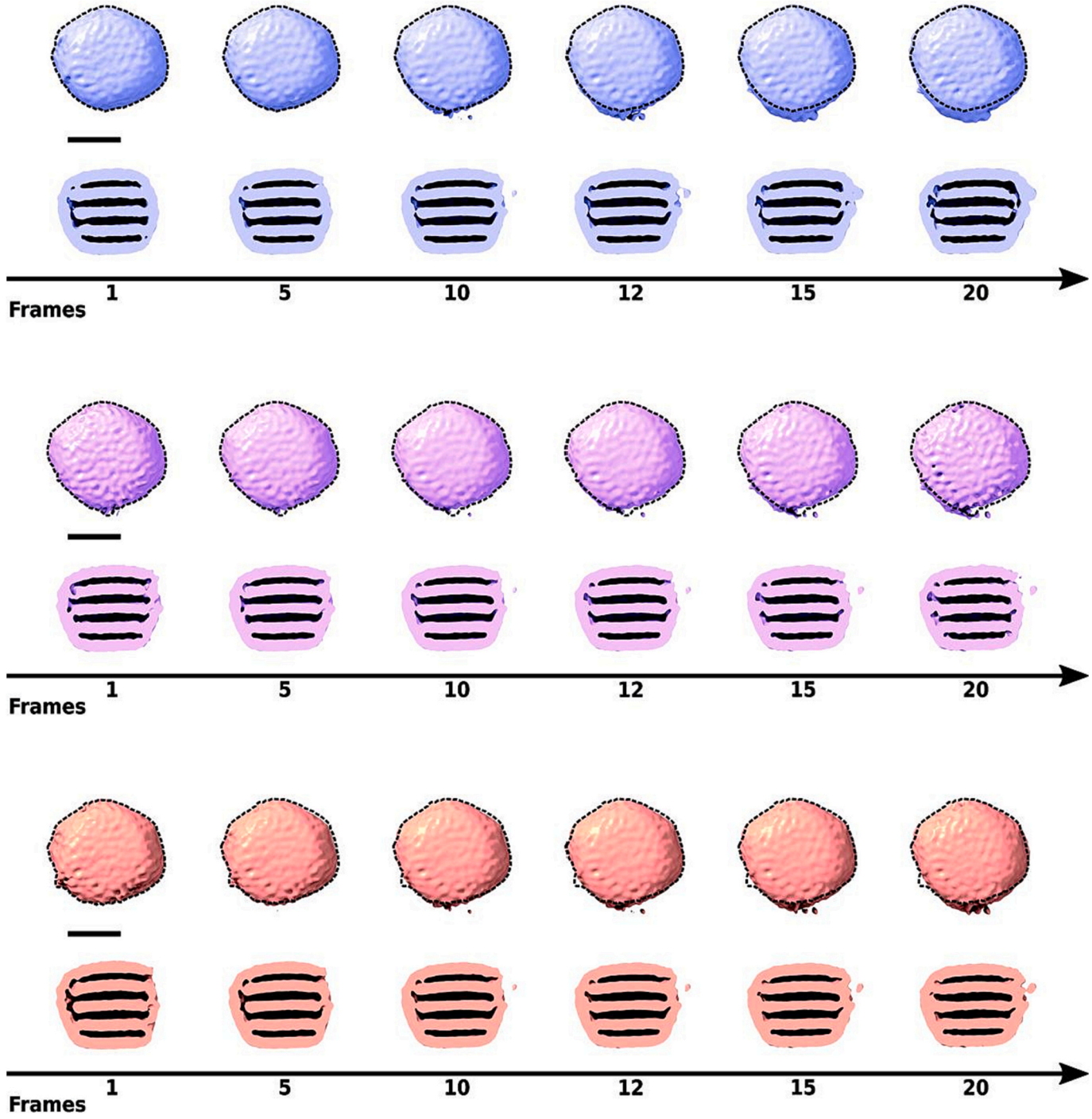

Fig. 9. Alignment of different frames from cryoSPARC 3DVA for three principal components. On the top view, the first volume is encircled by a black dashed line, which is repeated along all frames to have a comparison. Scale bar: 10 nm. 3D map images are produced with UCSF ChimeraX [68,69].

lipoprotein species – apo B-100 is non-exchangeable and follows the transition from VLDL to LDL. Understanding the basic principles that connect structure, dynamics and function in health and disease are still a great source of motivation for further studies. Comprehending structural and dynamical features will lead to a new understanding of the pathological mechanisms that lead to atherosclerosis and cardiovascular diseases and in turn will open new avenues for advanced drug discovery.

5. Materials and methods

5.1. Sample preparation

The sample preparation is described in detail in the Supporting Material. Briefly, CPD-buffered (citrate-phosphate-dextrose) human plasma was obtained from the Department of Blood Group Serology and Transfusion Medicine (Medical University of Graz, Austria), after written informed consent, according to a protocol approved by the Institutional Review Board of the Medical University of Graz. LDL isolation was done by several ultracentrifugation rounds. To select a highly

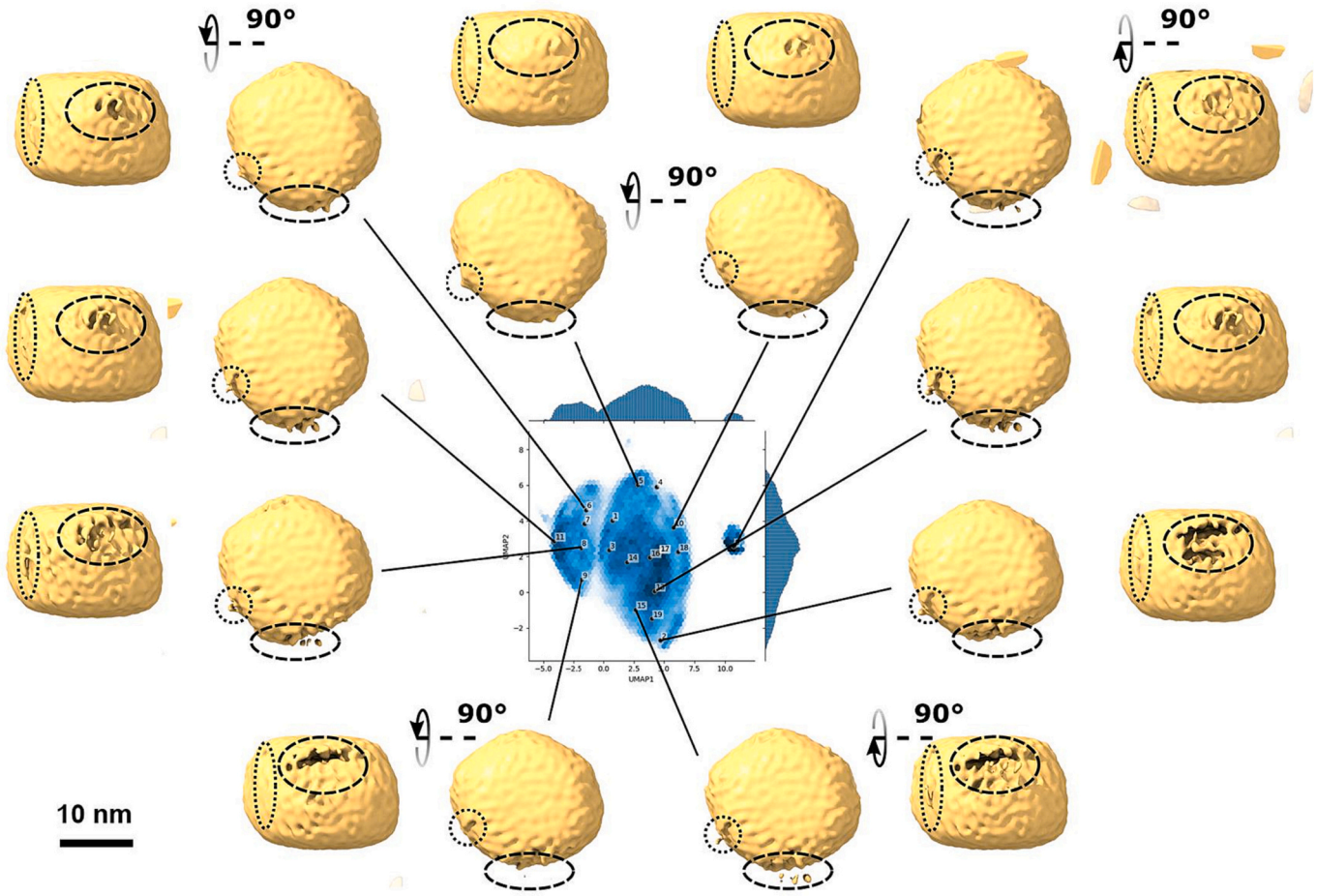

Fig. 10. Examples of 3D maps from cryoDRGN. In the center, UMAP representation of the latent space, where each point corresponds to one particle image. Top and front views are shown for all volumes. The "front" and "side" protrusions are encircled by a dashed and dotted line, respectively. Scale bar: 10 nm. 3D map images are produced with UCSF ChimeraX [68,69].

homogeneous population from an intrinsically heterogeneous pool of LDL particles, LDL was further subfractionated according to its density by Iodixanol density gradient ultracentrifugation [90]. Cryo-EM measurements were performed on an LDL subfraction with an estimated density of $\rho = 1.0286 \pm 0.004$ g/cm^3. Sample characterization was done using the following methods: SDS-PAGE (3.5 % gel, modified after Weber and Osborn), differential scanning calorimetry (DSC), and negative-staining transmission electron microscopy (TEM). The chemical composition of LDL was assessed with colorimetric assays. All details are presented in the Supporting Material (Table S1 and Figs. S6-S8).

5.2. Cryo-EM

5.2.1. Grid preparation

The grids were prepared and vitrified on the cryo-EM platform at the Institut Européen de Chimie et Biologie (IECB, Bordeaux, France). A carbon-coated grid R2/2300 mesh with a carbon layer of 2 nm was first glow-discharged for 30 s, with an intensity of 25 mA and a negative polarity, to make it hydrophilic. A volume of 4 μL of LDL sample with a protein concentration of c = 1 mg/mL was applied to the grid. Blotting and vitrification were automatically done in a Vitrobot Mark IV system (Thermo Fisher Scientific), with a blot time of 2 s and force 1, under 100 % humidity and temperature prior vitrification of $T = 4$ °C.

5.2.2. Data collection

The first screening was performed on a Talos Arctica (IECB, Bordeaux, France). Two subsequent data collections were carried out on the Titan Krios G3 at the CM01 beamline at the European Synchrotron Radiation Facility (ESRF, Grenoble, France) [91]. Parameters of each data collection are summarized in Table S2.

5.2.3. Image processing

The image processing was carried out using RELION 3.1 [92,93] and cryoSPARC v3.2 [61].

5.2.4. Motion correction and CTF estimation

First, motion correction was applied to the movies using the MOTIONCORR2 module from RELION. Estimation of the contrast transfer function (CTF) was conducted in RELION with the CTFFIND module [94] and in cryoSPARC with the patch-based CTF estimator.

5.2.5. Particle picking

In RELION, the particles on all micrographs were picked automatically using the templates generated from manually picked particles on a subset of micrographs. Additional sorting was performed with the calculation of a Z score [93], and discarding of all junk particles (Z score bigger than 1). In cryoSPARC, the template for automatic picking was a LDL 3D reconstruction computed prior from RELION. In both software packages, the picking parameters were optimized to reduce the number of false positives, while recovering enough particles. Subsequent sorting of the particles was conducted with several rounds of 2D classifications.

5.2.6. 2D classification

A specific procedure was followed in cryoSPARC for the 2D

classification, which is summarized in Fig. S1 of the Supporting Material. The two datasets collected on the Titan Krios were first processed separately and merged after a selection of 2D classes. Additional sorting of the particles was done with a 2D classification from all particles (around 700 k particles). From there, six 2D classes were selected, which present a good signal of the shell and visible protrusions of the LDL (see the densities designated by arrows in Fig. 1B-E), while ensuring to keep different views. This step aimed at isolating a representative subset of particles exhibiting these extra-densities of interest, while balancing the number of particles in the different views of the LDL.

Subsequent 2D classification of each of the six 2D classes was conducted, followed by a selection of classes with strong protrusion signal to achieve around 180 k particles in total.

5.2.7. 3D reconstruction

Ab initio reconstruction, followed by iterative refinement were processed in cryoSPARC [61] with the selected 180 k particles from the 2D classification, and then with the whole dataset (700 k particles) with the 180 k 3D reconstruction as reference. The resolution was estimated for all following maps by a post-processing job in RELION, using the FSC 0.143 criteria (see FSC curves in Fig. S10 of the Supporting Material). Sharpening was done with an ad-hoc B-factor of −500 Å^2, which was chosen following first estimations given by the 3D refinement.

5.2.8. 3D classification

Different strategies for the 3D classification or local refinement were followed in cryoSPARC. Finally, the whole dataset (700 k particles) was randomly split in 100 k batches, from which a 3D map was refined from the consensus map for each batch. 3D classification with K = 3 3D classes was then performed on each subset, with K being the number of classes. This resulted in around 25 classes, with <50 k particles in each of them. Close inspection of all classes led to a rough separation in three categories (termed S, F, and SF). Similar classes were then gathered and refined to create the three maps presented in Fig. 4, with their corresponding FSC shown in Fig. S10 (Supporting Material).

5.2.9. Variability analyses

Similar to the bootstrap analysis and the calculation of a 3D map variance on the LDL reconstruction by [38], LDL flexibility was explored in detail. For that purpose, the two main current algorithms for the study of continuous heterogeneity were applied. First, the 3D Variability Analysis (3DVA) from cryoSPARC [61] was applied using the three main components of the partial component analysis. For each component, a series of volumes (also termed as frames) was reconstructed along the so-called latent coordinate, which indicates where the volume is along the variability component. Secondly, the LDL reference map was processed in the package cryoDRGN (Deep Reconstructing Generative Networks), whose algorithm is based on neural networks [62,95].

CryoDRGN which parametrizes the structures and the conformational space is not handled by a linear description, as in contrary to 3DVA, and potentially accesses more complex variations. The corresponding dataset was trained first for 50 epochs, at dimension 8 for the latent variable z, as advised in [62]. From there, the latent space exhibited a huge cluster of particles and small subsets visualized as junk particles, which were thus removed. The remaining particles from the cluster were then submitted for an additional training, until 75 epochs, always at dimension 8.

5.2.10. Visualization

The 3D maps were displayed with UCSF ChimeraX [68,69], and the threshold value for all maps was chosen to enclose a volume of V = $3.325{\cdot}10^6$ Å^3, which corresponds to the theoretical volume of an LDL particle, as introduced in [35].

5.3. High speed atomic force microscopy

5.3.1. Measurement

Mica discs (V-1 grade muscovite mica sheets, NanoAndMore GmbH, Wetzlar, Germany) with a diameter of 1.5 mm were prepared and glued onto glass rods (2 mm diameter, 2 mm length, Hilgenberg GmbH, Malsfeld, Germany) with a two-component epoxy glue (UHU, Bolton Adhesives, Rotterdam, The Netherlands). A glass rod was glued onto the sample stage, using an acetone-diluted nail polish (Astor). After cleaving the mica disc, LDL with a protein concentration of 1.5 μg/mL in buffer (10 mM Tris/HCl, pH 7.4) was incubated for 3 min at RT and rinsed three times with 2 μL buffer. The sample stage was mounted into the liquid cell of the HS-AFM (RIBM, custom built after the design of Ando et al. [96]). For imaging, ultra-short cantilevers (USC-F1.2-k0.15–10, Nanoworld AG, Neuchâtel, Switzerland) with nominal spring constants of 0.1–0.15 N/m, resonance frequencies of ~500 kHz and a quality factor of ~2 were used. The free amplitude was set to ~3 nm and the setpoint amplitude to 85–90 %. Images were recorded on 100 nm × 100 nm areas with 256 × 256 pixels and scan rates of 239.59–315.15 ms/frame. The measurements were conducted at 22 °C.

5.3.2. Data analysis

To improve the visualization and smoothness of the particles, a Gaussian filter (σ = 0.8) was applied, using Kodec 4.4.7.39 (© 2006–2008 N. Kodera, M. Sakashita, M. Imai).

The resolution of AFM images is dependent on the radius of the used cantilever tip. As the tip is not infinitive thin, the scanned objects appear larger in the scanning direction. To compare the LDL dimensions measured with HS-AFM to the cryo-EM data, the real LDL diameters and protrusion widths were estimated by subtracting the tip effect using the following equation [77]:

$$\mathrm{FWHM} = 2\sqrt{d\left(R+\frac{d}{4}\right)}$$

where FWHM is the full width at half maximum of the LDL particle diameter or the width of the protrusion, R the radius of the cantilever tip (assumed to be 2 nm) and d the tip effect corrected diameter of the LDL particle or protrusion.

Statistical analysis was conducted as followed: The individual populations were tested for normal distribution (Shapiro Wilk test) and homogeneity of variances (Folded F test). If the populations were normal distributed and the variances were homogeneous, a *t*-test for independent samples was conducted (See Fig. S3 B - Boxplot LDL height), otherwise the non-parametric Mann-Whitney-*U* test was used (See Fig. S3 A - Boxplot LDL width).

Before tracking the LDL protrusions, the videos were drift-corrected using the "Image Stabilizer" plugin of Fiji [97] from Kang Li and Steven Kang (https://www.cs.cmu.edu/~kangli/code/Image_Stabilizer.html). To track the protrusion's mobility, the "Manual Tracking" plugin of Fiji was utilized (https://github.com/fiji/Manual_Tracking). The area of the protrusion's motion was calculated using the Fiji freehand selection and analysis tool.

Supplementary data to this article can be found online at https://doi.org/10.1016/j.ijbiomac.2023.126345.

Funding

This work was supported by the Foundation CFM through a JP Aguilar scholarship for the PhD thesis of A.C.; the Austrian Science Fund (FWF): project no. I 6211-B to K.K. and the Agence nationale de la recherche (ANR): project no. ANR-22-CE91-0003-01 to J.P.; the Amadeus project from Campus France [no. 42183RD] and accordingly the WTZ-grant by the OeAD [project no: FR 09/2019 and FR 05/2023]; S.S. holds a Ph.D. scholarship of the Austrian Science Fund (FWF) PhD program W1250 NanoCell; we acknowledge the Institut Universitaire de

France for providing J.P. additional time dedicated to research.

CRediT authorship contribution statement

Aline Cisse: Conceptualization, Methodology, Formal analysis, Investigation, Data curation, Visualization, Writing – original draft. **Ambroise Desfosses:** Methodology, Resources, Supervision, Writing – review & editing. **Sarah Stainer:** Investigation, Methodology, Formal analysis. **Eaazhisai Kandiah:** Investigation, Resources. **Daouda A.K. Traore:** Investigation, Resources. **Armel Bezault:** Investigation, Resources. **Anna–Laurence Schachner–Nedherer:** Resources, Writing – review & editing. **Gerd Leitinger:** Resources, Formal analysis, Supervision, Writing – review & editing. **Gerd Hoerl:** Investigation, Resources, Methodology. **Peter Hinterdorfer:** Resources, Supervision. **Irina Gutsche:** Resources, Writing – review & editing. **Ruth Prassl:** Conceptualization, Resources, Supervision, Project administration, Funding acquisition, Writing – review & editing. **Judith Peters:** Conceptualization, Investigation, Resources, Supervision, Project administration, Funding acquisition, Writing – review & editing. **Karin Kornmueller:** Conceptualization, Investigation, Resources, Visualization, Supervision, Project administration, Funding acquisition, Writing – review & editing.

Declaration of competing interest

The authors declare that they have no known competing financial interests or personal relationships that could have appeared to influence the work reported in this paper.

Data availability

The raw cryo-EM data associated with the current 3D maps will be deposited online (EMPIAR database, https://www.ebi.ac.uk/empiar/).

Acknowledgements

We thank Johann Krebs, Ivan Vidakovic, Robert Reimer and Gerhard Ledinski for their contribution in sample preparation, and the IT services of ILL for installation of the workstation (Holger Gebhard, Sylvain Dufour). We also thank Maria Bacia-Verloop for the tests on cryo-electron tomography and cryo-EM grid screening at the Glacios microscope of the IBS EM platform. The IBS EM platform is part of the Grenoble Instruct-ERIC center (ISBG; UMS 3518 CNRS-CEA-UGA-EMBL) within the Grenoble Partnership for Structural Biology (PSB), supported by FRISBI (ANR-10-INBS-05-02), and GRAL, financed within the University Grenoble Alpes graduate school (Ecoles Universitaires de Recherche) CBH-EUR-GS (ANR-17-EURE-0003). The electron microscope facility is supported by the Auvergne-Rhône-Alpes Region, the Fondation Recherche Médicale (FRM), the fonds FEDER, and the GIS-Infrastructures en Biologie Santé et Agronomie (IBISA). We acknowledge Guy Schoehn from the IBS EM platform for first beamtime and assistance. This work has benefited from the facilities and expertises of the Biophysical and Structural Chemistry platform (BPCS) at IECB, CNRS UMS3033, Inserm US001, Bordeaux University http://www.iecb.u-bordeaux.fr/index.php/fr/plateformestechnologiques. We acknowledge the European Synchrotron Radiation Facility for provision of beam time on CM01.

References

[1] H. Pownall, A.M. Gotto Jr., Human plasma apolipoproteins in biology and medicine, in: Structure and Function of Apolipoproteins, CRC Press, 1992, pp. 1–32.
[2] R. Prassl, P. Laggner, Molecular structure of low density lipoprotein: current status and future challenges, Eur. Biophys. J. Biophys. Lett. 38 (2) (2009) 145–158.
[3] T. Hevonoja, M.O. Pentikainen, M.T. Hyvonen, P.T. Kovanen, M. Ala-Korpela, Structure of low density lipoprotein (LDL) particles: basis for understanding molecular changes in modified LDL [in process citation], Biochim. Biophys. Acta 1488 (3) (2000) 189–210.
[4] M. Alakorpela, M.O. Pentikainen, A. Korhonen, T. Hevonoja, J. Lounila, P. T. Kovanen, Detection of low density lipoprotein particle fusion by proton nuclear magnetic resonance spectroscopy, J. Lipid Res. 39 (8) (1998) 1705–1712.
[5] A. Mehta, M.D. Shapiro, Apolipoproteins in vascular biology and atherosclerotic disease, Nat. Rev. Cardiol. 19 (3) (2022) 168–179.
[6] J. Borén, M.J. Chapman, R.M. Krauss, C.J. Packard, J.F. Bentzon, C.J. Binder, et al., Low-density lipoproteins cause atherosclerotic cardiovascular disease: pathophysiological, genetic, and therapeutic insights: a consensus statement from the European atherosclerosis society consensus panel, Eur. Heart J. 41 (24) (2020) 2313–2330.
[7] A.D. Sniderman, G. Thanassoulis, T. Glavinovic, A.M. Navar, M. Pencina, A. Catapano, et al., Apolipoprotein B particles and cardiovascular disease: a narrative review, JAMA Cardiol. 4 (12) (2019) 1287–1295.
[8] E. Di Angelantonio, N. Sarwar, P. Perry, S. Kaptoge, K.K. Ray, A. Thompson, et al., Major lipids, apolipoproteins, and risk of vascular disease, Jama. 302 (18) (2009) 1993–2000.
[9] C. Packard, M.J. Chapman, M. Sibartie, U. Laufs, L. Masana, Intensive low-density lipoprotein cholesterol lowering in cardiovascular disease prevention: opportunities and challenges, Heart. 107 (17) (2021) 1369–1375.
[10] A.J. Lusis, Atherosclerosis, Nature. 407 (6801) (2000) 233–241.
[11] H. Esterbauer, J. Gebicki, H. Puhl, G. Jürgens, The role of lipid peroxidation and antioxidants in oxidative modification of LDL, Free Rad Biol Med. 13 (1992) 341–390.
[12] B.J. Mckeone, J.R. Patsch, H.J. Pownall, Plasma triglycerides determine low-density-lipoprotein composition, physical-properties, and cell-specific binding in cultured-cells, J. Clin. Invest. 91 (5) (1993) 1926–1933.
[13] B.A. Griffin, D.J. Freeman, G.W. Tait, J. Thomson, M.J. Caslake, C.J. Packard, et al., Role of plasma triglyceride in the regulation of plasma low density lipoprotein (LDL) subfractions: relative contribution of small, dense LDL to coronary heart disease risk, Atherosclerosis. 106 (1994) 241–253.
[14] C. Packard, M. Caslake, J. Shepherd, The role of small, dense low density lipoprotein (LDL): a new look, Int. J. Cardiol. 74 (Suppl. 1) (2000) S17–S22.
[15] C.J. Packard, Small dense low-density lipoprotein and its role as an independent predictor of cardiovascular disease, Curr. Opin. Lipidol. 17 (4) (2006) 412–417.
[16] H. Yoshida, R. Kisugi, Mechanisms of LDL oxidation, Clin. Chim. Acta 411 (23–24) (2010) 1875–1882.
[17] D. Atkinson, R.J. Deckelbaum, D.M. Small, G.G. Shipley, Structure of human plasma low-density lipoproteins: molecular organization of the central core, Proc. Natl. Acad. Sci. U. S. A. 74 (1977) 1042–1046.
[18] R.J. Deckelbaum, G.G. Shipley, D.M. Small, Structure and interactions of lipids in human plasma low density lipoproteins, J. Biol. Chem. 252 (2) (1977) 744–754.
[19] K. Muller, P. Laggner, O. Glatter, G. Kostner, The structure of human-plasma low-density lipoprotein B. an X-ray small-angle scattering study, Eur. J. Biochem. 82 (1) (1978) 73–90.
[20] P. Laggner, G.M. Kostner, U. Rakusch, D.L. Worcester, Neutron small-angle scattering on selectively deuterated human plasma low density lipoproteins. The location of polar phospholipid headgroups, J. Biol. Chem. 256 (1981) 11832–11839.
[21] A. Johs, M. Hammel, I. Waldner, R.P. May, P. Laggner, R. Prassl, Modular structure of solubilized human apolipoprotein B-100. Low resolution model revealed by small angle neutron scattering, J. Biol. Chem. 281 (28) (2006) 19732–19739.
[22] R. Prassl, M. Pregetter, H. Amenitsch, M. Kriechbaum, R. Schwarzenbacher, J. M. Chapman, et al., Low density lipoproteins as circulating fast temperature sensors, PLoS One 3 (12) (2008), e4079.
[23] M. Papi, R. Brunelli, G. Ciasca, A. Maiorana, G. Maulucci, V. Palmieri, et al., Estradiol protective role in atherogenesis through LDL structure modification, J Phys D-Appl Phys. 49 (28) (2016) 9.
[24] S. Maric, T.K. Lind, J. Lyngso, M. Cardenas, J.S. Pedersen, Modeling Small-angle X-ray scattering data for low-density lipoproteins: insights into the fatty Core packing and phase transition, ACS Nano 11 (1) (2017) 1080–1090.
[25] B. Lehofer, M. Golub, K. Kornmueller, M. Kriechbaum, N. Martinez, G. Nagy, et al., High hydrostatic pressure induces a lipid phase transition and molecular rearrangements in low-density lipoprotein nanoparticles. particle & particle systems characterization: measurement and description of particle properties and behavior in powders and other disperse systems 35 (9) (2018).
[26] P. Laggner, The structure of plasma lipoproteins: evaluation by X-ray and neutron small-angle scattering, in: K.L. Mittal, B. Lindman (Eds.), Surfactants in Solution. 1, Plenum Publishing Corporation, New York, 1984, pp. 259–275.
[27] R. Prassl, J.M. Chapman, F. Nigon, M. Sara, S. Eschenburg, C. Betzel, et al., Crystallization and preliminary X-ray analysis of a low density lipoprotein from human plasma, J. Biol. Chem. 271 (46) (1996) 28731–28733.
[28] V.Y. Lunin, N.L. Lunina, S. Ritter, I. Frey, A. Berg, K. Diederichs, et al., Low-resolution data analysis for low-density lipoprotein particle, Acta Crystallogr D Biol Crystallogr. 57 (Pt 1) (2001) 108–121.
[29] C. Mikl, J. Peters, M. Trapp, K. Kornmueller, W.J. Schneider, R. Prassl, Softness of atherogenic lipoproteins: a comparison of very low density lipoprotein (VLDL) and low density lipoprotein (LDL) using elastic incoherent neutron scattering (EINS), J. Am. Chem. Soc. 133 (34) (2011) 13213–13215.
[30] M. Golub, B. Lehofer, N. Martinez, J. Ollivier, J. Kohlbrecher, R. Prassl, et al., High hydrostatic pressure specifically affects molecular dynamics and shape of low-density lipoprotein particles, Sci. Rep. 7 (2017) 46034.
[31] J. Peters, N. Martinez, B. Lehofer, R. Prassl, Low-density lipoproteins investigated under high hydrostatic pressure by elastic incoherent neutron scattering, Eur Phys J E Soft Matter. 40 (7) (2017) 68.

[32] J.E. Chatterton, M.L. Phillips, L.K. Curtiss, R.W. Milne, Y.L. Marcel, V. N. Schumaker, Mapping apolipoprotein B on the low density lipoprotein surface by immunoelectron microscopy, J. Biol. Chem. 266 (1991) 5955–5962.
[33] J.E. Chatterton, M.L. Phillips, L.K. Curtiss, R. Milne, J.C. Fruchart, V.N. Schumaker, Immunoelectron microscopy of low density lipoproteins yields a ribbon and bow model for the conformation of apolipoprotein b on the lipoprotein surface, J. Lipid Res. 36 (9) (1995) 2027–2037.
[34] J.M. Spin, D. Atkinson, Cryoelectron microscopy of low density lipoprotein in vitreous ice, Biophys. J. 68 (1995) 2115–2123.
[35] E.V. Orlova, M.B. Sherman, W. Chiu, H. Mowri, L.C. Smith, A.M. Gotto, Three-dimensional structure of low density lipoproteins by electron cryomicroscopy, Proc. Natl. Acad. Sci. U. S. A. 96 (15) (1999) 8420–8425.
[36] D.L. Gantz, M.T. Walsh, D.M. Small, Morphology of sodium deoxycholate-solubilized apolipoprotein B-100 using negative stain and vitreous ice electron microscopy, J. Lipid Res. 41 (9) (2000) 1464–1472.
[37] G. Ren, G. Rudenko, S.J. Ludtke, J. Deisenhofer, W. Chiu, H.J. Pownall, Model of human low-density lipoprotein and bound receptor based on cryoEM, Proc. Natl. Acad. Sci. U. S. A. 107 (3) (2010) 1059–1064.
[38] V. Kumar, S.J. Butcher, K. Oorni, P. Engelhardt, J. Heikkonen, K. Kaski, et al., Three-dimensional cryoEM reconstruction of native LDL particles to 16 angstrom resolution at physiological body temperature, PLoS One 6 (5) (2011).
[39] Y. Liu, luo D, Atkinson D., Human LDL core cholesterol ester packing: 3D image reconstruction and SAXS simulation studies, J. Lipid Res. (2010) 51.
[40] Y. Liu, D. Atkinson, Enhancing the contrast of ApoB to locate the surface components in the 3D density map of human LDL, J. Mol. Biol. 405 (1) (2011) 274–283.
[41] Y.H. Liu, D. Atkinson, Immuno-electron cryo-microscopy imaging reveals a looped topology of apoB at the surface of human LDL, J. Lipid Res. 52 (6) (2011) 1111–1116.
[42] P. Laggner, G. Degovics, K.W. Müller, O. Glatter, G.M. Kostner, A. Holasek, Molecular packing and fluidity of lipids in human serum low density lipoproteins, Hoppe-Seyler's Z Physiol Chem. 358 (1977) 771–778.
[43] P. Laggner, G.M. Kostner, G. Degovics, D.L. Worcester, Structure of the cholesteryl ester core of human plasma low density lipoproteins: selective deuteration and neutron small- angle scattering, Proc. Natl. Acad. Sci. U. S. A. 81 (1984) 4389–4393.
[44] M. Pregetter, R. Prassl, B. Schuster, M. Kriechbaum, F. Nigon, J. Chapman, et al., Microphase separation in low density lipoproteins. Evidence for a fluid triglyceride core below the lipid melting transition, J. Biol. Chem. 274 (3) (1999) 1334–1341.
[45] J.P. Segrest, M.K. Jones, V.K. Mishra, G.M. Anantharamaiah, D.W. Garber, ApoB-100 has a pentapartite structure composed of three amphipathic α-helical domains alternating with two amphipathic β-strand domains, Arterioscler. Thromb. 14 (1994) 1674–1685.
[46] J.P. Segrest, M.K. Jones, H. De Loof, N. Dashti, Structure of apolipoprotein B-100 in low density lipoproteins, J. Lipid Res. 42 (9) (2001) 1346–1367.
[47] K. Jeiran, S.M. Gordon, D.O. Sviridov, A.M. Aponte, A. Haymond, G. Piszczek, et al., A new structural model of apolipoprotein B100 based on computational modeling and cross linking, Int. J. Mol. Sci. 23 (19) (2022).
[48] C.J. Mann, T.A. Anderson, J. Read, S.A. Chester, G.B. Harrison, S. Kochl, et al., The structure of vitellogenin provides a molecular model for the assembly and secretion of atherogenic lipoproteins, J. Mol. Biol. 285 (1) (1999) 391–408.
[49] P.E. Richardson, M. Manchekar, N. Dashti, M.K. Jones, A. Beigneux, S.G. Young, et al., Assembly of lipoprotein particles containing apolipoprotein-B: structural model for the nascent lipoprotein particle, Biophys. J. 88 (4) (2005) 2789–2800.
[50] A. Sirwi, M.M. Hussain, Lipid transfer proteins in the assembly of apoB-containing lipoproteins, J. Lipid Res. 59 (7) (2018) 1094–1102.
[51] Z.G. Jiang, M. Carraway, C.J. McKnight, Limited proteolysis and biophysical characterization of the lipovitellin homology region in apolipoprotein B, Biochemistry. 44 (4) (2005) 1163–1173.
[52] G. McMullan, A.R. Faruqi, R. Henderson, Direct Electron detectors, Methods Enzymol. 579 (2016) 1–17.
[53] J. Frank, Advances in the field of single-particle cryo-electron microscopy over the last decade, Nat Protocols. 12 (2) (2017) 209–212.
[54] J.L. Vilas, N. Tabassum, J. Mota, D. Maluenda, A. Jiménez-Moreno, T. Majtner, et al., Advances in image processing for single-particle analysis by electron cryomicroscopy and challenges ahead, Curr. Opin. Struct. Biol. 52 (2018) 127–145.
[55] N. Thonghin, V. Kargas, J. Clews, R.C. Ford, Cryo-electron microscopy of membrane proteins, Methods. 147 (2018) 176–186.
[56] Y. Cheng, Membrane protein structural biology in the era of single particle cryo-EM, Curr. Opin. Struct. Biol. 52 (2018) 58–63.
[57] L. Bai, H. Li, Cryo-EM structures of the endoplasmic reticulum membrane complex, FEBS J. 289 (1) (2022) 102–112.
[58] C.C. Su, M. Lyu, C.E. Morgan, J.R. Bolla, C.V. Robinson, E.W. Yu, A 'Build and Retrieve' methodology to simultaneously solve cryo-EM structures of membrane proteins, Nat. Methods 18 (1) (2021) 69–75.
[59] M.T. Doyle, J.R. Jimah, T. Dowdy, S.I. Ohlemacher, M. Larion, J.E. Hinshaw, et al., Cryo-EM structures reveal multiple stages of bacterial outer membrane protein folding, Cell. 185 (7) (2022), 1143-56.e13.
[60] X. Yao, X. Fan, N. Yan, Cryo-EM analysis of a membrane protein embedded in the liposome, Proc. Natl. Acad. Sci. U. S. A. 117 (31) (2020) 18497–18503.
[61] A. Punjani, J.L. Rubinstein, D.J. Fleet, M.A. Brubaker, cryoSPARC: algorithms for rapid unsupervised cryo-EM structure determination, Nat. Methods 14 (3) (2017) 290–296.
[62] E.D. Zhong, T. Bepler, B. Berger, J.H. Davis, CryoDRGN: reconstruction of heterogeneous cryo-EM structures using neural networks, Nat. Methods 18 (2) (2021) 176–185.
[63] T. Ando, High-speed atomic force microscopy, Curr. Opin. Chem. Biol. 51 (2019) 105–112.
[64] T. Sakurai, S. Takeda, J.Y. Takahashi, Y. Takahashi, N. Wada, S. Trirongjitmoah, et al., Measurement of single low-density lipoprotein particles by atomic force microscopy, Ann. Clin. Biochem. 50 (Pt 6) (2013) 564–570.
[65] C.Y. Gan, M.Y. Ao, Z.H. Liu, Y. Chen, Imaging and force measurement of LDL and HDL by AFM in air and liquid, FEBS Open Bio. 5 (2015) 276–282.
[66] K. Wang, Y. Li, C. Luo, Y. Chen, Dynamic AFM detection of the oxidation-induced changes in size, stiffness, and stickiness of low-density lipoprotein, J Nanobiotechnology. 18 (1) (2020) 167.
[67] M. Axmann, E. Sezgin, A. Karner, J. Novacek, M.D. Brodesser, C. Röhrl, et al., Receptor-independent transfer of low density lipoprotein cargo to biomembranes, Nano Lett. 19 (4) (2019) 2562–2567.
[68] T.D. Goddard, C.C. Huang, E.C. Meng, E.F. Pettersen, G.S. Couch, J.H. Morris, et al., UCSF ChimeraX: meeting modern challenges in visualization and analysis, Protein Sci. 27 (1) (2018) 14–25.
[69] E.F. Pettersen, T.D. Goddard, C.C. Huang, E.C. Meng, G.S. Couch, T.I. Croll, et al., UCSF ChimeraX: structure visualization for researchers, educators, and developers, Protein Sci. 30 (1) (2021) 70–82.
[70] G.S. Ginsburg, M.T. Walsh, D.M. Small, D. Atkinson, Reassembled plasma low density lipoproteins. Phospholipid-cholesterol ester-apoprotein B complexes, J. Biol. Chem. 259 (10) (1984) 6667–6673.
[71] M. Shepelenko, A. Hirsch, N. Varsano, F. Beghi, L. Addadi, L. Kronik, et al., Polymorphism, structure, and nucleation of Cholesterol.H(2)O at aqueous interfaces and in pathological media: revisited from a computational perspective, J. Am. Chem. Soc. 144 (12) (2022) 5304–5314.
[72] W. Sattler, G.M. Kostner, G. Waeg, H. Esterbauer, Oxidation of lipoprotein Lp(a). A comparison with low-density lipoproteins, Biochim. Biophys. Acta 1081 (1991) 65–74.
[73] S. Kim, J. Chen, T. Cheng, A. Gindulyte, J. He, S. He, et al., PubChem 2023 update, Nucleic Acids Res. 51 (D1) (2023). D1373-D80.
[74] I. Ermilova, A.P. Lyubartsev, Cholesterol in phospholipid bilayers: positions and orientations inside membranes with different unsaturation degrees, Soft Matter 15 (1) (2018) 78–93.
[75] H. Ohvo-Rekila, B. Ramstedt, P. Leppimaki, J.P. Slotte, Cholesterol interactions with phospholipids in membranes, Prog. Lipid Res. 41 (1) (2002) 66–97.
[76] L.R. Pan, J.P. Segrest, Computational studies of plasma lipoprotein lipids, Biochimica Et Biophysica Acta-Biomembranes. 1858 (10) (2016) 2401–2420.
[77] C. Lamprecht, J. Strasser, M. Köhler, S. Posch, Y.J. Oh, R. Zhu, et al., Biomedical sensing with the atomic force microscope, in: B. Bhushan (Ed.), Nanotribology and Nanomechanics: An Introduction, Springer International Publishing, Cham, 2017, pp. 135–173.
[78] K. Teilum, J.G. Olsen, B.B. Kragelund, Functional aspects of protein flexibility, Cell. Mol. Life Sci. 66 (14) (2009) 2231–2247.
[79] M. Grimaldo, F. Roosen-Runge, F. Zhang, F. Schreiber, T. Seydel, Dynamics of proteins in solution, Q. Rev. Biophys. 52 (2019).
[80] T.H.D. Nguyen, W.P. Galej, X.C. Bai, C. Oubridge, A.J. Newman, S.H.W. Scheres, et al., Cryo-EM structure of the yeast U4/U6.U5 tri-snRNP at 3.7 Å resolution, Nature. 530 (7590) (2016) 298–302.
[81] T. Nakane, D. Kimanius, E. Lindahl, S.H. Scheres, Characterisation of molecular motions in cryo-EM single-particle data by multi-body refinement in RELION, Elife. (2018) 7.
[82] D.J. Benton, A. Nans, L.J. Calder, J. Turner, U. Neu, Y.P. Lin, et al., Influenza hemagglutinin membrane anchor, Proc. Natl. Acad. Sci. U. S. A. 115 (40) (2018) 10112–10117.
[83] F. Martino, M. Pal, H. Muñoz-Hernández, C.F. Rodríguez, R. Núñez-Ramírez, D. Gil-Carton, et al., RPAP3 provides a flexible scaffold for coupling HSP90 to the human R2TP co-chaperone complex, Nat. Commun. 9 (1) (2018) 1501.
[84] A. von Appen, J. Kosinski, L. Sparks, A. Ori, A.L. DiGuilio, B. Vollmer, et al., In situ structural analysis of the human nuclear pore complex, Nature. 526 (7571) (2015) 140–143.
[85] B.W. Hoogenboom, L.E. Hough, E.A. Lemke, R.Y.H. Lim, P.R. Onck, A. Zilman, Physics of the nuclear pore complex: theory, modeling and experiment, Phys Rep. 921 (2021) 1–53.
[86] K. Henzler-Wildman, D. Kern, Dynamic personalities of proteins, Nature. 450 (7172) (2007) 964–972.
[87] J. Peters, M.T. Giudici-Orticoni, G. Zaccai, M. Guiral, Dynamics measured by neutron scattering correlates with the organization of bioenergetics complexes in natural membranes from hyperthermophile and mesophile bacteria, Eur Phys J E Soft Matter. 36 (7) (2013) 78.
[88] A. Cisse, A.-L. Schachner-Nedherer, M. Appel, C. Beck, J. Ollivier, G. Leitinger, et al., Dynamics of apolipoprotein B-100 in interaction with detergent probed by incoherent neutron scattering, The Journal of Physical Chemistry Letters. 12 (51) (2021) 12402–12410.
[89] L. Wang, M.T. Walsh, D.M. Small, Apolipoprotein B is conformationally flexible but anchored at a triolein/water interface: a possible model for lipoprotein surfaces, Proc. Natl. Acad. Sci. U. S. A. 103 (18) (2006) 6871–6876.
[90] G. Hörl, H. Froehlich, U. Ferstl, G. Ledinski, J. Binder, G. Cvirn, et al., Simvastatin efficiently lowers Small LDL-IgG immune complex levels: a therapeutic quality beyond the lipid-lowering effect, PLoS One 11 (2) (2016), e0148210.
[91] E. Kandiah, T. Giraud, Antolinos A. de Maria, F. Dobias, G. Effantin, D. Flot, et al., CM01: a facility for cryo-electron microscopy at the European synchrotron, Acta Crystallogr D Struct Biol. 75 (Pt 6) (2019) 528–535.
[92] S.H. Scheres, A Bayesian view on cryo-EM structure determination, J. Mol. Biol. 415 (2) (2012) 406–418.

[93] S.H. Scheres, RELION: implementation of a Bayesian approach to cryo-EM structure determination, J. Struct. Biol. 180 (3) (2012) 519–530.
[94] A. Rohou, N. Grigorieff, CTFFIND4: fast and accurate defocus estimation from electron micrographs, J. Struct. Biol. 192 (2) (2015) 216–221.
[95] Zhong ED, Bepler T, Davis JH, Berger B. Reconstructing continuous distributions of 3D protein structure from cryo-EM images 2019 September 01, 2019:[arXiv: 1909.05215 p.]. Available from: https://ui.adsabs.harvard.edu/abs/2019arXiv190905215Z.
[96] T. Ando, N. Kodera, Y. Naito, T. Kinoshita, K. Furuta, Y.Y. Toyoshima, A high-speed atomic force microscope for studying biological macromolecules in action, Chemphyschem. 4 (11) (2003) 1196–1202.
[97] J. Schindelin, I. Arganda-Carreras, E. Frise, V. Kaynig, M. Longair, T. Pietzsch, et al., Fiji: an open-source platform for biological-image analysis, Nat. Methods 9 (7) (2012) 676–682.